Flexible cross-correlated (C2) imaging method for the modal content characterization in a broad range of wavelengths

Muliar, Olena; Usuga Castaneda, Mario A.; Michieletto, Mattia; Kristensen, Torben; Alkeskjold, Thomas T.; Rottwitt, Karsten; Lægsgaard, Jesper

Published in:
Optics Express

Link to article, DOI:
10.1364/OE.25.005521

Publication date:
2017

Document Version
Publisher's PDF, also known as Version of record

Research Article | Vol. 25, No. 5 | 6 Mar 2017 | OPTICS EXPRESS 5521

Optics EXPRESS

Flexible cross-correlated (C^2) imaging method for the modal content characterization in a broad range of wavelengths

OLENA MULIAR,[1,*] MARIO A. USUGA,[1] MATTIA MICHIELETTO,[2] TORBEN KRISTENSEN,[2] THOMAS T. ALKESKJOLD,[2] KARSTEN ROTTWITT,[1] AND JESPER LÆGSGAARD[1]

[1]*DTU Fotonik, Department of Photonics Engineering, Technical University of Denmark, Ørsteds Plads, 2800 Kgs. Lyngby, Denmark*
[2]*NKT Photonics, Blokken 84, 3460 Birkerød, Denmark*
[*]*omul@fotonik.dtu.dk*

Abstract: We demonstrate a flexible cross-correlated (C^2) imaging method in the time domain by application of a tunable and highly flexible light source. An advantage of the flexible C^2 method is shown by characterization of the step-index fiber (SMF28) over a broad range of wavelengths from 870nm to 1090nm and by the modal analysis of the distributed modal filtering (DMF) rod fiber within a wavelength range from 1050nm to 1090nm. Also, the influence of the spectral shape and bandwidth on the imaging trace is investigated by deliberately adjusting the input spectrum of the light source. The modal intensity as well as the phase distribution are extracted by the alternative method of 2D FT filtering. Being exceptionally tunable the flexible C^2 method gives an ability to adapt the system's parameters in a desired manner satisfying even measurements of very specific fiber designs opening up new possibilities for advanced modal characterization of fibers over broad range of wavelengths.

OCIS codes: (120.3180) Interferometry; (060.2270) Fiber characterization; (120.2650) Fringe analysis.

References and links

1. R.-J. Essiambre and R. W. Tkach, "Capacity trends and limits of optical communication networks," Proc. IEEE **100**(5), 1035–1055 (2012).
2. N. K. Fontaine, R. Ryf,H. Chen, A. V. Benitez, J. E. Antonio Lopez, R. Amezcua Correa, B. Guan, B. Ercan, R. P. Scott, S. J. Ben Yoo, L. Gruner-Nielsen, Y. Sun, and R. J. Lingle, "30x30 MIMO transmission over 15 spatial modes," in *Optical Fiber Communication Conference, OFC 2015*, Th5C.1.
3. T. Mori, T. Sakamoto, M. Wada, T. Yamamoto, and F. Yamamoto, "Few-mode fibers supporting more than two LP modes for mode-division-multiplexed transmission with MIMO DSP," J. Lightwave Technol. **32** (14), 2468–2479 (2014).
4. T. T. Alkeskjold, M. Laurila, L. Scolari, and J. Broeng, "Single-mode ytterbium-doped large-mode-area photonic bandgap rod fiber amplifier," Opt. Express **19**(8), 7398–7409 (2011).
5. S. Wielandy,"Implications of higher-order mode content in large mode area fibers with good beam quality," Opt.Express **15**(23), 15402–15409 (2007).
6. J. W. Nicholson, A. D. Yablon, S. Ramachandran, and S. Ghalmi, "Spatially and spectrally resolved imaging of modal content in large-mode-area fibers," Opt. Express **16**(10), 7233–7243 (2008).
7. H. - J. Otto, F. Jansen, F. Stutzki, C. Jauregui, J. Limpert, and A. Tünnermann, "Improved modal reconstruction for spatially and spectrally resolved imaging," J. Lightwave Technol. **31**(8), 1295–1299 (2013).
8. R. A. Barankov, "Cross-correlation imaging for waveguide characterization," M. S. Thesis, http://arxiv.org/abs/1206.0666v1 [physics.optics] 24.
9. D. N. Schimpf, R. Barankov, and S. Ramachandran, "Cross-correlated (C2) imaging of fiber and waveguide modes," Opt. Express **19**(14), 13008–13019 (2011).
10. J. Demas and S. Ramachandran, "Sub-second mode measurement of fibers using C2 imaging," Opt. Express **22**(19), 23043–23056 (2014).
11. D. N. Schimpf and S. Ramachandran, "Polarization-resolved imaging of an ensemble of waveguide modes," Opt. Lett. **37**(15), 3069–3071 (2012).
12. F. Kong, G. Gu, T. W. Hawkins, J. Parsons, M. Jones, and C. Dunn, "Quantitative mode quality characterization of fibers with extremely large mode areas by matched white-light interferometry," Opt. Express **22**(12), 14657–14665 (2014).

#281618 https://doi.org/10.1364/OE.25.005521
Journal © 2017 Received 29 Nov 2016; revised 27 Jan 2017; accepted 31 Jan 2017; published 1 Mar 2017

Optics EXPRESS

13. M. Laurila, R. Barankov, M. M. Jørgensen, T. T. Alkeskjold, J. Broeng, J. Lægsgaard, and S. Ramachandran,"Cross-correlated imaging of single-mode photonic crystal rod fiber with distributed mode filtering," Opt. Express **21**(8), 9215–9229 (2013).
14. J. Plucinski, R. Hypszer, P. Wierzba, M. Strakowski, M. Jedrzejewska-Szczerska, M. Maciejewski, and B. B. Kosmowski, "Optical low-coherence interferometry for selected technical applications," Bull. Pol. Ac.:Tech. **56**(2), 155–172 (2008).
15. M. Born, E. Wolf, *Principles of Optics* (Cambridge University, 1999).
16. B. E. A. Saleh, C. M. Teich *Fundamentals of Photonics* (Wiley-Interscience, 2013)
17. S. Nakadate and H. Saito, "Fringe scanning speckle-pattern interferometry," Appl. Opt. **24**(14), 2172–2180 (1985).
18. T. Fricke-Begemann and J. Burke, "Speckle interferometry: three-dimensional deformation field measurement with a single interferogram," Appl. Opt. **40**(28), 5011–5022 (2001).
19. G. Pedrini, I. Alexeenko, W. Osten, and H. J. Tiziani, "Temporal phase unwrapping of digital hologram sequences," Appl.Opt. **42**(29), 5846–5854 (2003).
20. Y. Fu, G. Pedrini, and W. Osten "Vibration measurement by temporal Fourier analyses of a digital hologram sequence," Appl.Opt. **46**(23), 5719–5727 (2007).
21. M. Takeda, H. Ina, and S. Kobayashi, "Fourier-transform method of fringe-pattern analysis for computer-based topography and interferometry," J. Opt. Soc. Am. B 72(1), 156–160 (1982).
22. M. Hipp, J. Woisetschlager, P. Reiterer, and T. Neger, "Digital evaluation of interferograms," Meas. **36**(1), 53–66 (2004).
23. Thorlab's, "Single Mode Fiber with Ø900 m Hytrel Jacket," https://www.thorlabs.com/drawings/ed76fbde27c25cdc-62510C47-5056-0103-794C6E46F8B7E137/SMF-28-100-SpecSheet.pdf.
24. NKT Photonics, "Application note: Supercontinuum Generation in Photonics Crystal Fibers," http://www.nktphotonics.com/wp-content/uploads/2015/02/Application_note_-_Supercontinuum-General1.pdf.
25. NKT Photonics, "Data sheet: SuperK EXTREME," http://www.nktphotonics.com/wp-content/uploads/2015/05/superk-extreme.pdf.
26. NKT Photonics,"Data sheet: Super Select," http://www.nktphotonics.com/wp-content/uploads/2015/03/SuperK_SELECT.pdf.
27. M. M. Jørgensen, S. R. Petersen, M. Laurila, J. Lægsgaard, and T. T. Alkeskjold, "Optimizing single mode robustness of the distributed modal filtering rod fiber amplifier," Opt. Express **20**(7), 7263–7373 (2012).

1. Introduction

Higher-order modes (HOMs) acquired considerable attention from scientists and researchers all over the world during the last decade. The expected capacity crunch of modern communication systems in the nearest future [1] leads to an extensive investigation of alternative technologies to increase capacity of the common fiber links. In this perspective, HOMs due to their unique features come out as distinct spatial channels for data transmission [2] and appear as potential candidates and a key element of the newly proposed multiplexing technology [3]. However, in some distinct applications, for instance, systems of high power pulse amplification and delivery [4] the presence of HOMs is extremely undesired, since HOMs can lead to pointing instability and fluctuating peak intensity, as well as reduce beam quality [5]. In any aforesaid scenarios, determination of HOMs presence and their experimental verification at the output of a fiber gives the opportunity to bring the system to a higher operational level by carefully predicting its performance. A technique for modal content analysis which is robust and easy in implementation is highly desired and a beneficial diagnostic tool for characterization of fiber-based systems. Among up-to-date developed methods of fiber mode detection interference-based imaging techniques have already contributed significant results [6–12].

One of the examples of a valuable method that allows recovery of the fiber modal content, spatial phase and modal intensity distribution of the modes as well as modal dispersion properties is the spatially and spectrally resolved imaging technique (S^2) [6]. There currently exist two approaches for the S^2 method: with a swept-laser and camera and the raster-scanning approaches. Both setups are robust and simple. However, time consumption for the raster-scanning approach,for example, and the requirement of one propagating mode being dominant for both approaches, limit the method. Several reported theoretical algorithms [7] can help to overcome S^2 limitation, but for the present they are not confirmed experimentally.

Optics EXPRESS

Another powerful tool for reconstruction of the fiber modes is cross-correlated imaging (C^2) that can be performed in the time [8, 9] as well as in the frequency [10] domain. Both methods provide information about modal content, intensity distributions of the modes and their relative group-delays. Furthermore, with a small variation of the setup configuration and data analysis of the C^2 method in the time domain polarization-sensitive measurement of the modal content can be performed [11]. As a modification of cross-correlated imaging the white-light interferometry method reported in [12] can be considered. Here a highly resolvable time resolution is achieved by the application of the same test fiber in both arms of the interferometer, which precisely matches the residual group velocity dispersion and permits resolving of the modal group delays on the scale of few femtoseconds. It worth mentioning how significant all aforesaid techniques are, especially, for evaluation of the modal content of a fiber of specific design, for example, as a large mode area (LMA) fiber, that is of high importance for high-power fiber amplifiers. Demonstration of the modal content analysis of such LMA fiber was reported in [13], where the distributed modal filtering (DMF) rod fiber was evaluated by the C^2 method in the time domain applying a light source of the fixed narrow spectral width.

However, neither of those techniques carries out the full overview of the fiber modal behavior along a broad range of wavelengths. In this paper we present an flexible technique of cross-correlated imaging for the fiber mode detection that enables measuring of modal characteristics in a broad range of wavelengths giving a deep insight into the modal development at different wavelengths. Modal intensity distributions as well as modal phase profiles and differential time delays are provided. Moreover, being exceptionally flexible the described setup configuration of the optimized C^2 method gives an ability to adjust the system's parameters to meet the requirements of specific fiber designs.

2. Theory

The technique of cross-correlated (C^2) imaging is based on a principle of low-coherence interferometry (LCI) or white light interferometry (WLI). Here information about physical quantities of interest is extracted with regard to the change of an optical path difference (OPD) of two interfering beams [14]. In the case of C^2 imaging the setup is based on a Mach-Zehnder interferometer (MZI). The general scheme of the setup is depicted in Fig. 1. Light beams from a light source are divided into both arms of the interferometer. Light in the sample arm is coupled into the fiber under test (FUT), where several modes propagate. By a delay line in the reference arm an optical path length (OPL) of the reference beam is changed, until it matches the OPL of the desired mode in the FUT. After recombination on a beam splitter, beams are directed onto the camera, that takes pictures of interacting beams at each step of the delay line displacement. An interferogram is obtained from the set of the interference pictures represented as a change of intensity recorded by the camera depending on the time delay introduced by the delay line in the reference arm. It contains information about about the fiber modal content. The interference pattern consists of the set of fringes, that appear when optical path differences (OPDs) between the specific modes in the FUT and the fundamental mode (FM) in the reference fiber are matched. The interference intensity reaches its maximum, when the values of OPD is close to zero. Positions of those maxima correspond to the positions of every specific mode at the line of time delays gained by the delay line. Determining the time delay of HOMs relative to the FM the differential modal time delays can be found. The change of intensity taken by the camera along the entire range of the time-delays consists of two terms: a background intensity $I_0(x, y)$ and an interference intensity $I_{Int}(x, y, \tau)$.

$$I = I_0(x, y) + I_{Int}(x, y, \tau) \tag{1}$$

where (x, y) are positions of pixels in a picture, $I_0(x, y)$ is the background intensity, which is a sum of the intensities radiated from the reference and the sample arms. For the collimated beams

Optics EXPRESS

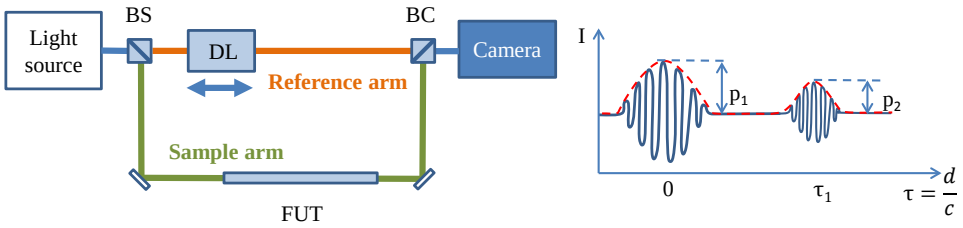

(a) (b)

Fig. 1. (a) The scheme of the setup is presented as an unbalanced Mach-Zehnder interferometer. BS and BC are a beam splitter and a beam combiner, FUT is a fiber under test and DL is a delay line. (b) An example of the cross-correlated trace, where the intensity1 recorded by a camera is represented as function of the time-delay τ.

it does not depend on the time delay τ.

$$I_0 = I_r(x,y) + I_s(x,y) \tag{2}$$

$I_r(x,y)$ and $I_s(x,y)$ are taken by the camera, when only one of the beams is pointed at the camera, and another one is blocked. The interference intensity $I_{Int}(x,y,\tau)$ is presented through the cross-correlation function $c_{rm}(\tau-\tau_m)$:

$$I_{Int}(x,y,\tau) = \sum_m 2\sqrt{I_r(x,y)I_m(x,y)}\alpha_m|c_{rm}(\tau-\tau_m)|cos(\Psi) \tag{3}$$

$$c_{rm}(t) = \frac{1}{2\pi}\int S(\Omega)exp(i\Delta\phi_{mr}(\Omega))exp(-i\Omega t)\mathrm{d}\Omega \tag{4}$$

where α_m is the real modal weight, τ_m is the relative time delay between the FM and the definite HOM in the FUT, $|c_{rm}(\tau-\tau_m)|$ is a modulus of the cross-correlation function, Ψ is a linear phase that describes the fast oscillation behavior and the phase mismatch between the two arms of the interferometer. Equation (4) expresses the dependence of the cross-correlation function on the spectrum of the input light source $S(\Omega)$ and the residual dispersion mismatch between two arms of the interferometer $\Delta\phi_{mr}(\Omega)$. Frequency Ω is a shifted frequency corresponding to a central frequency ω_0.

$$\Omega = \omega - \omega_0 \tag{5}$$

Equations (3) and (4) constitute the basis of the data analysis of the C^2 method and were derived in [8, 9]. The modulus of the cross-correlation function $|c_{rs}(\tau-\tau_m)|$ describes an envelope of the intensity oscillation and represents the cross-correlation trace (C^2 imaging trace, red curve in Fig. 1(b)). Analyzing a stack of images acquired by the camera at every pixel at each step of the delay line d, extracting the background intensity I_0 and normalizing to the intensity of the reference beam, one obtains the cross-correlation signal $\mathcal{P}(\mathbf{r},\tau)$:

$$\mathcal{P}(\mathbf{r},\tau) = \sum_m \alpha_m^2|c_{rm}(\tau-\tau_m)|I_m(\mathbf{r}) \tag{6}$$

that encodes information about the modal weight $p_m = \alpha_m^2$, the modal intensity $I_m(\mathbf{r})$ and the differential time delay between modes τ_m.

Detailed information about the mode determination is obtained following the procedure described in [8] and [9]. The number of peaks at the cross-correlated trace obtained from the

Optics EXPRESS

recorded interferograms, schematically described in [Fig. 1(b)], corresponds to the quantity of modes that propagate in the FUT. The amplitude of peak defines the real modal weight, while the position of each peak is interpreted as a differential modal time delay τ_m of the specific mode m relative to the FM. Integrating the interference signal $\mathcal{P}(\mathbf{r}, \tau)$ over a definite extent in time over each pixel on the imaging plane, the intensity distribution of each mode I_m can be decomposed.

3. Decomposition of modal content with 2D Fourier transform

The concept of interferogram analysis employing the Fourier transform is widely known within the fields of speckle interferometry [17, 18] and holography [19, 20]. The basis of the current approach for fringe-pattern analysis was reported in 1982 by Mitsuo Takeda [21]. Following its procedure a phase map was extracted from a single recorded interferogram that was Fourier transformed and undesired terms were isolated, while the required sideband was shifted and centered at zero frequency. The phase map was picked up, when derived term was inverse Fourier transformed.

In a case,when interferograms are recorded by a CCD camera a two-dimensional Fourier transform (2D FT) for the fringe pattern analysis is used. The spatial intensity distribution of the fringe pattern is expressed in the form [22]:

$$I(x, y) = I_0(x, y) + m(x, y)cos[2\pi f_0 x + \phi(x, y)] \tag{7}$$

where $\phi(x, y)$ is the phase of the interest, $I_0(x, y)$ is the background intensity distribution and $m(x, y)$ is a contrast function, x and y is a position of pixels on the imaging plane, f_0 is a spatial carrier frequency along x direction that is proportional to the angle θ introduced between two interfering beams and in the case of small angle can be expressed:

$$f_0 = k_1 - k_2 \approx k_0(\theta_1 - \theta_2) = k_0\theta \tag{8}$$

where k_1, k_2 are the wave numbers of the corresponding interfering beams, θ is an introduced angle between beams.

Following complex notation Eq. (7) can be rewritten as:

$$I(x, y) = I_0(x, y) + c(x, y)e^{2\pi i f_0 x} + c^*(x, y)e^{-2\pi i f_0 x} \tag{9}$$

where

$$c(x, y) = \frac{1}{2}m(x, y)e^{i\phi(x,y)} \tag{10}$$

Applying 2D Fourier transform to Eq. (9) with respect to x one obtains:

$$I(f_x, f_y) = I_0(f_x, f_y) + C(f_x - f_0, f_y) + C^*(f_x + f_0, f_y) \tag{11}$$

where $I_0(f_x, f_y)$, $C(f_x - f_0, f_y)$ and $C^*(f_x + f_0, f_y)$ are spatial Fourier spectra separated by the carrier frequency f_0 from each other. $C(f_x + f_0, f_y)$ and $I_0(f_x, f_y)$ can be removed by using a filter centered at f_0. In this case, the larger angle between the interfering beams, the larger f_0 and the more separate the spatial Fourier spectra in reciprocal space are. Shifting $C(f_x - f_0, f_y)$ to the origin $C(f_x, f_y)$ the carrier frequency f_0 is eliminated. Employing the inverse Fourier transform to $C(f_x, f_y)$ with respect to f_x, $c(x, y)$ is derived, from which the phase $\phi(x, y)$ can be extracted.

The described approach can easily be implemented for the modal content analysis by C^2 imaging technique. To obtain the fringe pattern at the camera plane at the output of the interferometer an angle was introduced between beams from the reference and the sample arms.The created fringes are described by Eq. (3) derived in the previous section. The fact that the beams from reference and sample arms interfere at the camera plane after traveling with a relative angle

Optics EXPRESS

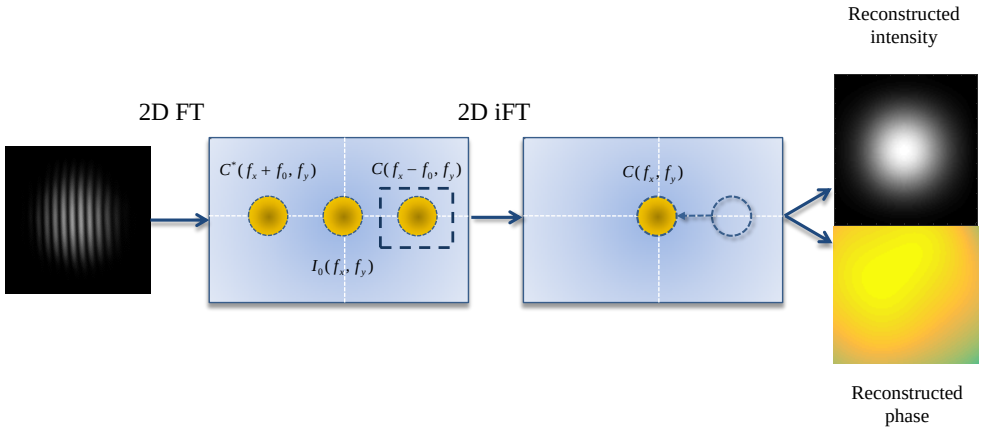

Fig. 2. The scheme of 2D FT analysis of the fiber modal content.

between them, introduces an extra term with linear phase that is added to Ψ in the cosine in Eq. (3). It is important to notice that the angle between the beams (and therefore the extra linear phase term) is known by the experimentalist and is completely under her/his control.

To characterize fiber modal content by 2D FT from the C^2 imaging trace we use the interferograms at the time $\tau = \tau_m$ that corresponds to the maxima of interference peaks at the trace. Each of the collected fringe patterns is analyzed following the aforesaid method. The scheme of analysis is described in Fig. 2. At the beginning the background intensity $I_0(x, y)$ and intensity distribution of the reference beam $I_r(x, y)$ is filtered by 2D FT. The outcome term $c(x, y)$ contains information about the modal intensity distribution in its real part and the modal phase distribution encoded into the phase angle of $c(x, y)$. Applying the phase unwrapping algorithm the phase distribution of the corresponding mode can be acquired.

4. Description of the method for the flexible C^2 imaging

Dispersion has a crucial importance for the temporal resolution of all interferometric imaging techniques, especially when broadband sources are used as input light sources.It arises from the dependence of the propagation constant on the frequency when light propagates in a dispersive medium, as a fiber. An important aspect of C^2 imaging is the ability to balance dispersion, minimizing its influence on results of measurements. It is achieved by the careful matching of the reference fiber and the FUT in the following way [8]:

$$L_r = \frac{\beta_m^{(2)}}{\beta_r^{(2)}} L \tag{12}$$

where L_r and L are the lengths of the reference fiber and the FUT, $\beta_r^{(2)}$ and $\beta_m^{(2)}$ are the second-order coefficients of a Taylor expansion of the mode propagation constant β around the central frequency ω_0. It is worth mentioning that the group-velocity dispersion (GVD) is precisely matched for the FM in the FUT, while HOMs are still affected by the residual dispersion that leads to broadening of the modal peaks at the C^2 imaging trace. Another important parameter that has to be taken into account is the spectral bandwidth of the input light source. To reach a high temporal resolution for C^2 imaging an optimal spectral width of the light source has to be chosen.

As it was described previously, Eq. (4) shows the correlation between the C^2 trace appearance and the group-delay dispersion $\Delta\phi_{mr}(\Omega)$ as well as the input spectrum $S(\Omega)$. The last two

Optics EXPRESS

parameters determine the temporal resolution of the cross-correlation trace.

When the influence of dispersion is minimized ($\Delta\phi_{mr} \approx 0$) the temporal resolution of the system is mainly governed by the coherence time of the light source $\Delta\tau_{FWHM}^{coher} = 8 \cdot ln(2)/\Delta\Omega$, where $\Delta\Omega$ is the FWHM of the input pulse and $\Delta\tau_{FWHM}$ is the FWHM of the interference peak at the imaging trace. In this case, an increase of the spectral bandwidth for the seed source allows to obtain a better temporal resolution. On the other hand, if the interferometer is not balanced and the residual GVD is large, the temporal resolution is affected by dispersive broadening $\Delta\tau_{FWHM}^{disp} = \Delta\phi_{mr}(\Omega) \cdot \Delta\Omega$ and increase of the spectral bandwidth causes degradation of the resolution. However, to cancel dispersion completely for all modes simultaneously is impossible, consequently a compromise between the residual dispersion and a spectrum width has to be found. Furthermore, between the spectral shape and the shape of the C^2 imaging trace exists a direct dependence as well. The smooth bell-shaped (Gaussian shape) spectrum leads to the smooth cross-correlation trace, while the steep edges in the spectrum, for example, caused by implementation of a bandpass filter result in artifacts at the imaging trace around interference peaks that affects the data analysis. Therefore, deliberate selection of an appropriate bandwidth of the seed source and the setup components are a high concern for the C^2 imaging technique.

The scheme of the setup for the flexible cross-correlated imaging is shown in Fig. 3. As a light source we used the supercontinuum laser *SuperK EXTREME*, the output of which was filtered by a multi-line tunable filter *SuperK Select*, both produced by *NKT Photonics*. *SuperK EXTREME* emits light within the range of wavelengths from 400nm to 2400nm, while *SuperK Select* scans along the near infrared wavelengths from 800nm to 1400nm with filter bandwidth of 7.23nm.An aforesaid spectral width corresponds to one excited channel of *SuperK Select* or in other words, one excited beam with a central wavelength deliberately chosen along the range of scanned wavelengths. The measured spectrum of one beam at the central wavelength of 1050nm is depicted in Fig. 4 and has a characteristic sinc-shape. *Super Select* and *SuperK EXTREME* are independent products of *NKT Photonics* and additional information can be found in [24–26]. The principle of operation of *SuperK EXTREME* is based on a supercontinua generation that is formed when a photonic crystal fiber is pumped by a ps 1064nm laser at wavelength close to zero dispersion wavelength, while *Super Select* is an acousto-optic tunable filter, principle of operation of which is based on an acousto-optic diffraction in an optically anisotropic medium.

One of the powerful features of *SuperK Select* in combination with *SuperK EXTREME* is an opportunity to add up to 8 emitting channels at the output increasing in this way the spectral bandwidth of the seed source at the input of the C^2 setup. The power of each channel of *SuperK Select* can be individually controlled and modified. In Fig. 4, for instance, the beam power was adjusted to 30% of the maximum power, that results in the sidelobes suppression up to -10dB in comparison with the main peak. Power modulation allows shaping of the input spectrum in any desired way. The tunable spectral width together with adjustable spectral shape, create a unique opportunity for optimization of the C^2 imaging method making it a flexible diagnostic tool with a high degree of variability of parameters that can easily be adjusted for the measurement of fibers with particular designs.

5. Demonstration of the method

To demonstrate the elegance and simplicity of the method we chose a standard step-index fiber SMF28 of 1m length as the FUT, that was balanced by the same length of a single mode fiber 980HP as the reference fiber. Operational wavelengths chosen for the measurement are from 870nm to 1090nm. Current selection of wavelengths was determined due to an operational window of the setup components. To predict the appearance of the C^2 imaging trace we made a model of SMF28. At the desired wavelengths the FUT is considered as a few-mode fiber, where only the FM and the first HOM group are supported. Calculation confirms presence of two modes along the entire range of wavelengths of our interest. Dependence of the effective refractive

Optics EXPRESS

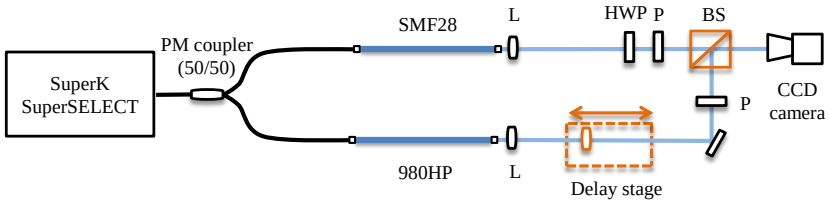

Fig. 3. The scheme of the measurement setup for the flexible C^2 imaging. L - lens, HWP - half-wave plate, P - polarizer, BS - beams splitter, CCD - the camera.

indices for LP01 and LP11 versus wavelength is shown in Fig. 5. Close to the wavelength of 1279nm LP11 experiences cutoff and is not confined anymore within the fiber core. This is in agreement with the provided fiber specifications [23].

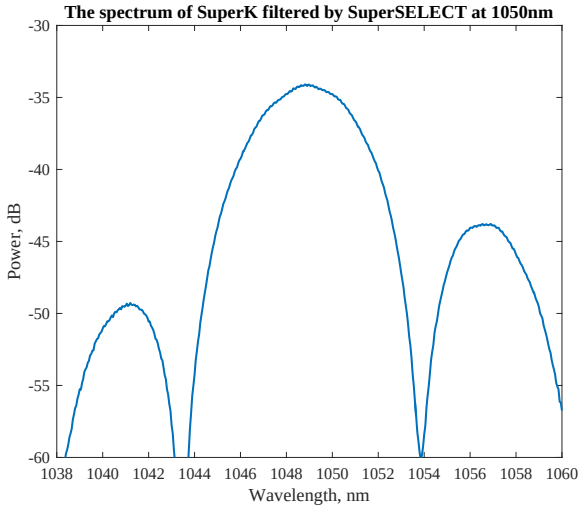

Fig. 4. The output spectrum of SuperK filtered by SuperSELECT at 1050nm, when the only one channel is turned on.

To investigate the influence of the spectral shape and width on the temporal resolution and appearance of the C^2 imaging trace we performed measurement of SMF28 with diverse input spectra from the seed source. Combinations of the merged input beams and their total FWHM are presented in Table 1.

Table 1. Combination of beams from *SuperSELECT* used in the measurements.

Number of beams	Wavelengths, nm	Spectral width, nm
1 beam	1050nm	7.23nm
2 beams	1040nm-1050nm	4nm and 5nm
2 beams	1045nm-1050nm	9nm
3 beams	1045nm-1050nm-1055nm	14nm
5 beams	1042nm-1046nm-1050nm-1054nm-1058nm	16.93nm
8 beams	1042nm-1045nm-1048nm-1050nm-1052nm-1055nm-1058nm-1061nm	28.25nm

Optics EXPRESS

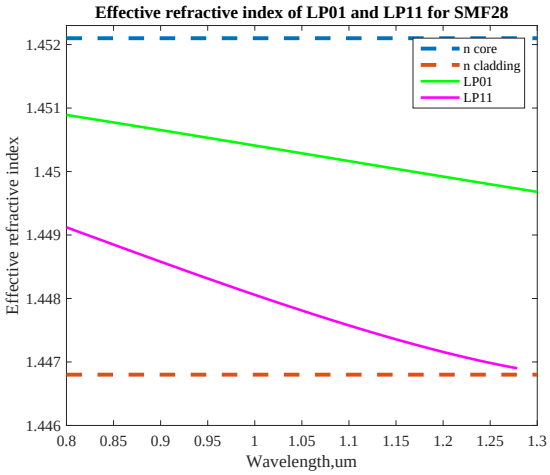

Fig. 5. Calculated effective refractive indices for the FM and the first HOM as a function of wavelength for SMF28. LP11 experience the cutoff around 1260nm and is not guided at longer wavelengths.

Thus, spectra created from 1, 2, 3,5 and 8 beams were used. Figure 6(a) demonstrates selected spectra taken at the wavelength of 1050nm. Wavelength of the characteristic peak at 1064nm corresponds to the wavelength of the laser pump. Spectra that include the wavelength of the pump peak can be affected by its power, but when the level of the pump peak is sufficiently suppressed it does not corrupt the shape of the total spectrum and hence it does not affect the imaging trace. It is also worth taking into account that excitation of the beams in close proximity to each other (less than 4nm between channels) especially close to the pump peak wavelength introduces noise between the channels that originated from the RF signal from the RF drive that powers *SuperSelect*. The noise is clearly seen at the spectrum of 8 beams at 1050nm [Fig. 6(b)]. Moving to the shorter wavelengths the influence of the pump peak as well as fluctuation in the spectrum is reduced, for example, the same beam combination at 890nm [Fig. 6(b)] experiences lower interaction noise between the channels than at 1050nm.

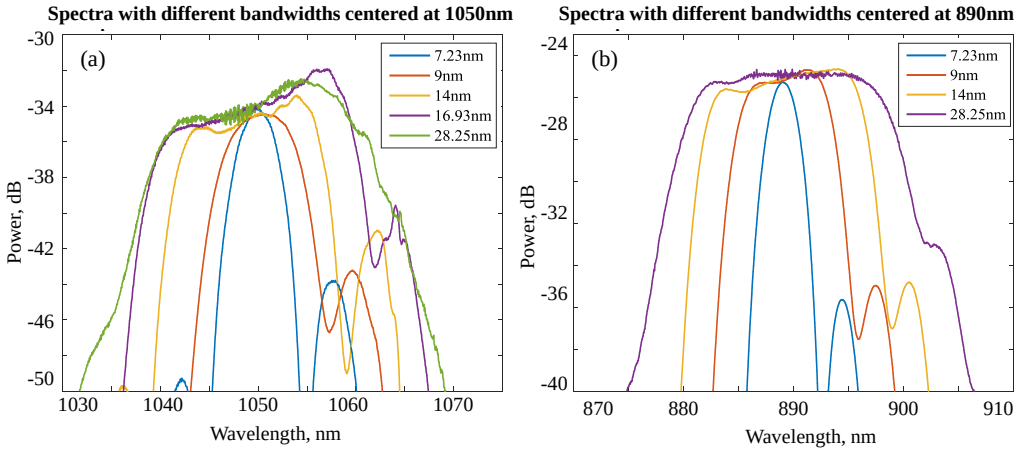

Fig. 6. The output spectrum of *SuperK* filtered by *SuperSELECT* with different FWHM centered at 1050nm (a) and 890nm (b).

Optics EXPRESS

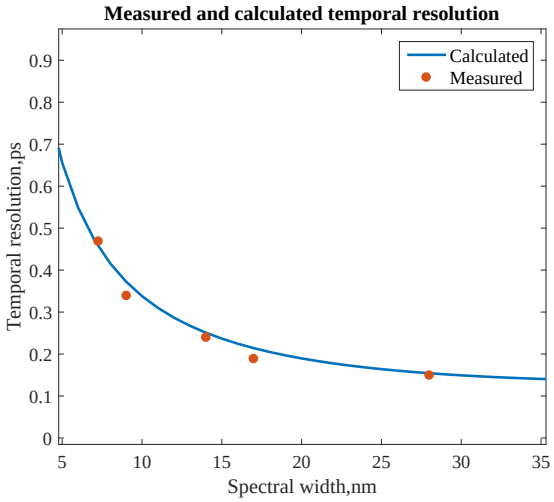

Fig. 7. Calculated and measured temporal resolution depending on the different spectral widths of the input spectrum at the central wavelength of 1050nm.

During the experiments the input spectral width was varied from 7.23nm to 28.25nm. Dependence of the temporal resolution on the spectral width is presented in Fig. 7. Here the blue curve corresponds to the calculated values and the red one to the temporal resolution obtained during the measurements as a full-width half maximum of the interference peak for LP01 at the C^2 trace. For the input spectrum merged from 8 beams the measured temporal resolution is 0.15ps and the calculated value is 0.154ps, while for the spectrum of 1 beam, presented in Fig. 4, the predicted value is 0.465ps and the measured is 0.47ps. In Fig. 8 two C^2 imaging traces are depicted measured at 1050nm with the highest and the lowest temporal resolution.

An example of the spectral shape influence on the C^2 trace appearance is shown in Fig. 9, where the input spectrum was combined from 2 channels with spectra centered at the wavelengths of 1040nm and 1050nm. Individual spectra of each channel resembles in the shape the spectrum depicted in Fig. 4, while the spectral shape of two combined channels with separation of 10nm is shown as inset in Fig. 9. Due to the split shape of the resultant spectrum of the two joined channels, the interference peaks acquire characteristic sinc-shape with strong undesirable sidelobes. Consequently, the the combined spectrum from channels with separation of the central wavelengths larger than the FWHM of the single channel, here more than 7nm, results in artifacts on the imaging trace in the form of the sidelobes around each interference peak.

During the measurements the delay line was programmed to scan with an increment of 5μm that corresponds to 16fs of the time delay along 1mm distance. Such incremental step and scanning distance allow us to resolve LP01 and LP11 at the C^2 trace along the entire range of chosen wavelengths and for the all selected spectra. The first order HOM is excited in the FUT by positioning the input beam relative to the fiber core, so the input coupling condition is changed and light power is distributed between the FM and the HOMs. At the beginning two modes were detected at 1050nm with the modal power close to 60% and 40% corresponding to LP01 and LP11 [Fig. 8]. Detected modal power demonstrates one of the advantages of the C^2 imaging method to reveal the modes with equal or close to equal modal power.The positions of the peaks on the trace specify the temporal delay of HOM with respect to the FM. At wavelength of 1050nm measured differential time delay between modes is -2ps/m, while the predicted value is -1.92ps/m. At the range of wavelengths from 870nm and up to its cutoff, LP11 propagates faster than LP01 due to higher group velocity, and during the measurements it comes out as a first

Optics EXPRESS

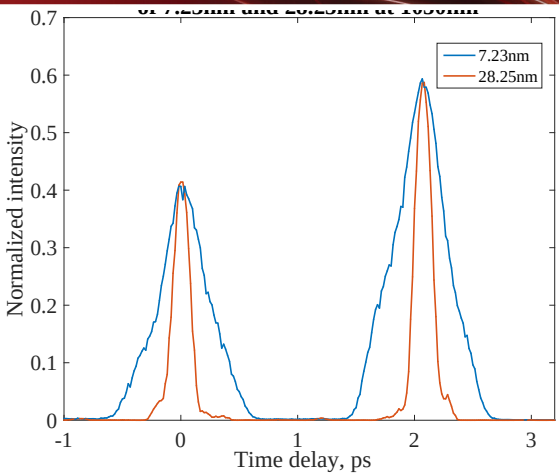

Fig. 8. Comparison of the C^2 traces measured with the spectral bandwidths of 7.23nm (blue line) and 28.25nm (red line) at the wavelength of 1050nm.

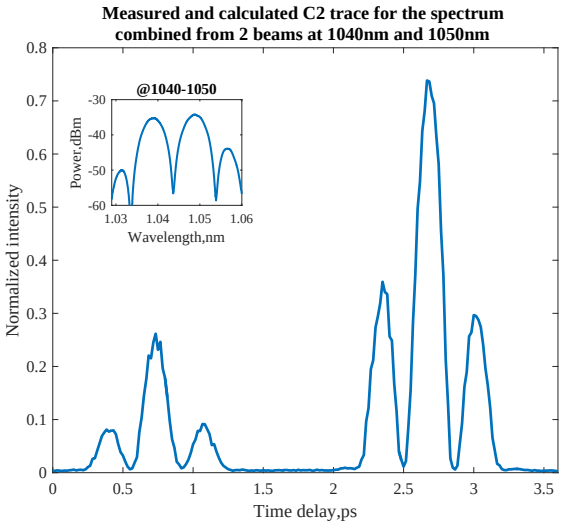

Fig. 9. The measured C^2 trace for the spectrum combined with 2 beams at the central wavelengths of 1040nm and 1050nm. At the inset is depicted the input spectrum.

arriving mode at the C^2 trace. Expected turn around point in the group velocities of the modes is around 870nm. To investigate modal behavior at shorter wavelength tuned input spectrum merged of 8 channels were implemented further for the C^2 characterization of the fiber modal content.

6. Results of C^2 measurement at different wavelengths

As it was shown in the previous section an unique feature of the setup for the flexible cross-correlated imaging is an opportunity to perform measurements at any desired wavelength from 870nm to 1090nm due to implementation of the broadband light source (*SuperK*) in combination with the tunable filter (*SuperSELECT*). The 8-beams spectrum described in Table 1 with power in each channel 60%-80%-100%-90%-90%-70%-50%-30% and shown in [Fig. 6(a)] as a green curve was translated to central wavelengths 870nm, 930nm, 970nm, 1030nm, 1050nm and 1090nm and used for estimation of the SMF28 modal contents. From the C^2 traces recorded at the aforesaid wavelengths we extracted the differential time delay between LP01 and LP11 that

Optics EXPRESS

is presented in Fig. 10 as a function of wavelength.

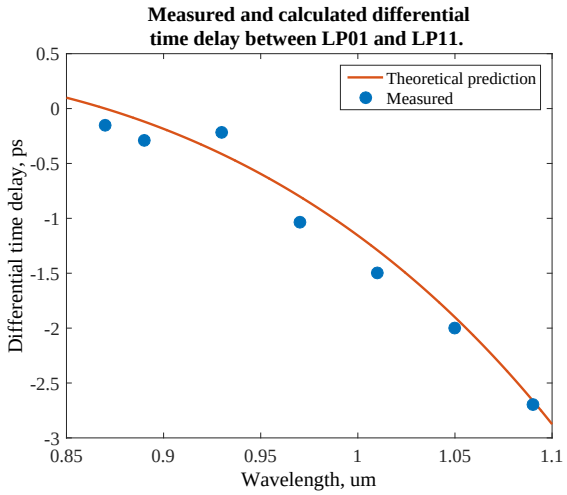

Fig. 10. Calculated and measured differential time delay between LP01 and LP11 propagating in the FUT.

Red curve is a calculated estimation, while blue dots are the measured data. As it can be seen, experimental and measured values are in a good agreement. It is noticeable how the differential time delay between two modes decreases approaching zero value at wavelength close to 870nm. Down to 930nm an intermodal time delay between detected modes was large enough to resolve them even with the smallest input spectrum bandwidth of 7.23nm, while approaching the turn-around point it is beneficial to increase the temporal resolution of the system to the maximum using the widest bandwidth of 28,25nm. The imaging traces taken for the two extreme bandwidths of the input spectrum at the central wavelength of 890nm are demonstrated in [Fig. 11(a)]. The recorded C^2 trace with a narrow input spectrum of 7.23nm, that consists of 1 beam, has lower temporal resolution and at 890nm it is already impossible to resolve modes, since they coincide with one another [blue curve in Fig. 11(a)].

The temporal resolution improvement of the imaging trace is reached by implementation of the input spectrum with a wider spectral bandwidth of 28.25nm. Measurement of the C^2 trace with 8 merged channels mentioned in Table 1 at 890nm gives clear identification of the propagating LP01 and LP11 modes. Moreover, the intensity profiles and the spatial phase profiles are extracted and depicted at the insets. LP01 has a characteristic flat phase distribution, while between the lobes of LP11 there is change close to π in the phase. Abrupt jump of 2π at the reconstructed phase distribution of LP11 at wavelength of 870nm is an artifact that appears due to the poor interferogram quality at that wavelength, since it is the edge of the operational window of the input fiber coupler, and the beams intensity distribution and power from the reference and the sampling arms are not the same.

With the optimized configuration of the setup and the reached temporal resolution of 0.15ps we are able to resolve propagating modes at the wavelength of 870nm close to their turn around point. The cross-correlated trace recorded at 870nm is presented in [Fig. 11(b)]. Here LP11 appears as a superimposed shoulder on LP01. Two modes coincide with each other, nevertheless they can be decomposed. Intensity and phase profiles are depicted as the insets in [Fig. 11(b)]. The sharp edge in the lower part of the extracted phase distribution of LP11 appears due to the error in the phase unwrapping. LP11 remains the fastest mode at the imaging trace at 870nm

Optics EXPRESS

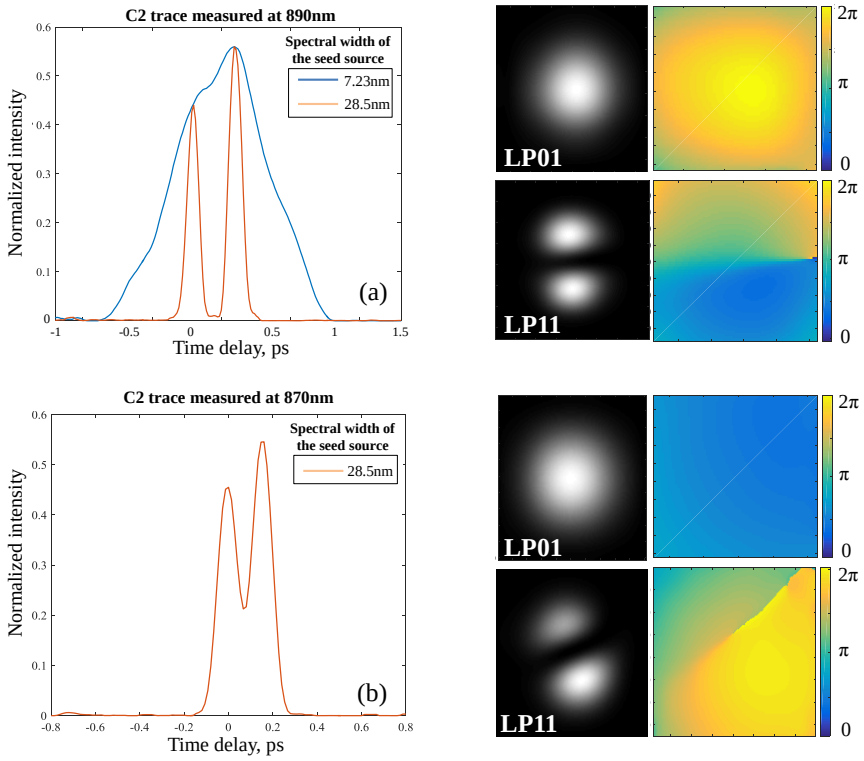

Fig. 11. The C^2 trace recorded at the central wavelength of 890nm (a) with spectral widths of 7.23nm (blue line) and 28.25nm (red line) and 870nm (b) with spectral width of 28.25nm (red line). As wavelength was varied the relative modal power was maintained to be kept constant. Insets on the right side represent reconstructed modal intensity profiles of LP01 and LP11 at the maxima of the interference peaks and corresponding phase distributions zoomed in the area of interest.

and still possesses higher group velocity than LP01. The relative time delay between modes is -0.15ps. Results of the measurement show that the turn around wavelength for LP01 and LP11 in the SMF28 is lower than the calculated value. However, restriction of the operational wavelength window of the components in the C^2 setup does not permit us to go below 870nm.

To demonstrate the benefit of the flexible cross-correlated method in the time domain and the opportunity to tune the system in a desired manner according to the specific fiber designs the modal content of the passive pure-silica core distributed modal filtering (DMF) rod fiber, manufactured for 1064nm single-mode operation, was evaluated within a wavelength range from 1050nm to 1090nm. Current type of a rod fiber was in details described in [4] and [27]. Due to unique design of the DMF rod fiber it has three regimes of operation: single mode (SM), multimode (MM) and leaky mode (LM) regime over a specific range of wavelengths [4, 27]. The FM is well-guided in the core in the SM regime with high suppression of HOMs due to the resonant cladding structure [27].The DMF rod fiber becomes slightly multimode for wavelengths longer than the SM bandwidth, where the core overlap of the HOM gradually increases. On the other hand, for wavelengths shorter than the SM bandwidth, there is a small range of wavelengths where the FM experiences a drop in the power, due to coupling to the resonators in the inner cladding structure (LM regime). Investigation of modal regimes of the DMF rod fiber with the C^2 method was performed in [13]. However, due to a light source, that was applied during the

Optics EXPRESS

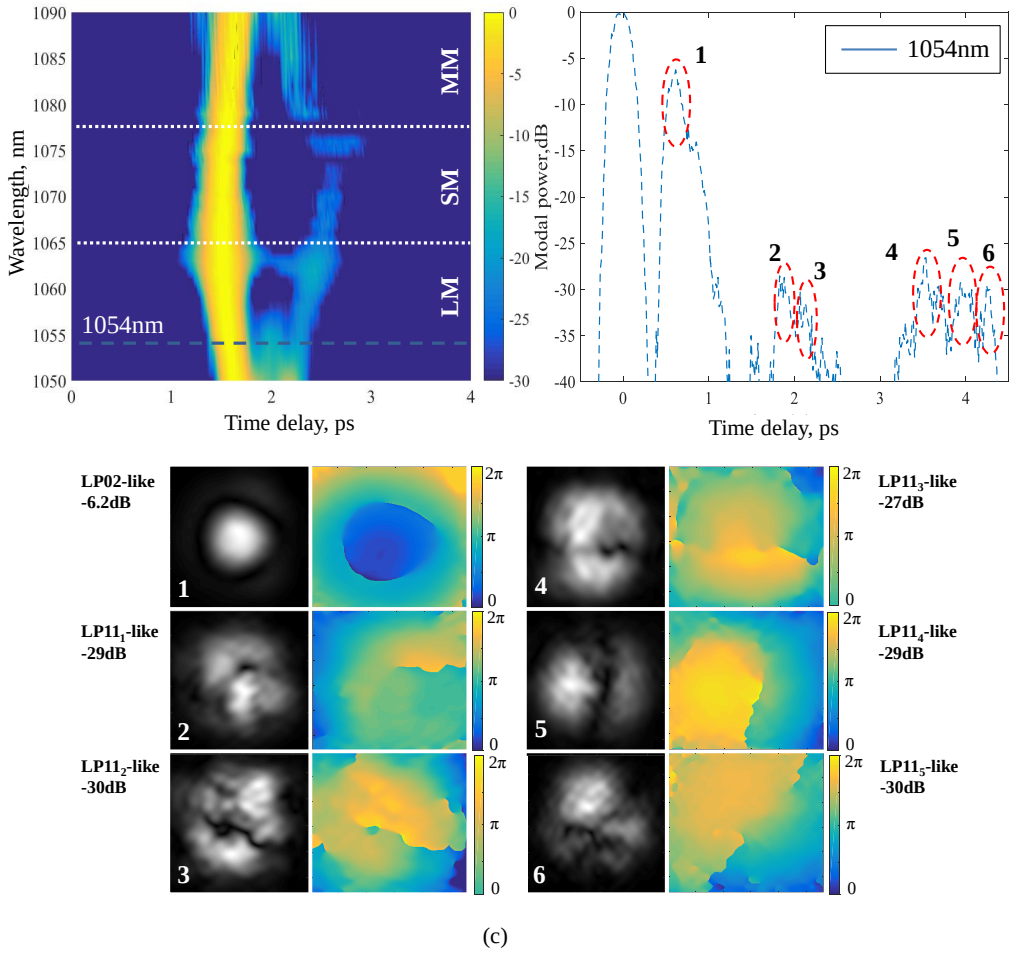

(c)

Fig. 12. (a) A spectrogram of the intermodal time delay vs wavelength. Every horizontal line on the spectrogram corresponds to a C2 measurement with the spectrum centered on a specific wavelength. (b) The cross-correlated trace measured with offset coupling at 1054nm. (c) Reconstructed modes presented at the measured C^2 trace.

measurements, fixed at 1050nm, wavelength tuning was achieved by an angle-tunable bandpass filter [13], limiting flexibility of the modal analysis. Our modification of the C^2 setup due to a tunable source, than can scan a larger range of wavelengths, gives much better flexibility for the analysis of all 3 regimes of operation of the DMF rod fiber. We evaluated the modal content of the rod fiber by performing C^2 measurements at each wavelength of our interest from 1050nm to 1090nm. Based on the measurements, the SM regime of operation is determined from the most offset that was introduced during different measurements and established at a wavelength range, where the power of HOMs is suppressed more than -20dB relative to the FM. Since the DMF rod fiber operates in 3 distinct regimes, it is also important to find an appropriate bandwidth and a spectral shape of the seed source to obtain a smooth C^2 trace and still to be able to resolve modes with a small intermodal delays without a considerable influence from the spectral overlap with other regimes. We scanned 1m of the DMF rod fiber with an input spectrum bandwidth of 15nm, merged from 3 channels with separation of 4nm between each channel.[Figure 12(a)] depicts a spectrogram that shows a dependence of the intermodal group delay on wavelength, when a certain offset was introduced to excite LP02-like mode in the region of the LM regime. According to the spectrogram depicted in [Fig. 12(a)] the SM regime is present at wavelengths

Optics EXPRESS

from approximately 1065nm to 1078nm. However, the ranges of the SM regime are depend on an amount of an introduced offset and can be underestimate due to the influence of the spectral overlap with the MM and LM regimes [13]. To evaluate the modal content within the leaky wavelength region was introduced an additional even larger offset to the input coupling and the C^2 measurement was performed at wavelength of 1054nm. The resultant imaging trace is present in [Fig. 12 (b)]. As a consequence of the additionally introduced offset, on the C^2 trace are present 6 HOMs, 5 of which are suppressed below cutoff level. Reconstructions of the modal intensity and the phase distribution are depicted in [Fig. 12 (c)]. It is obvious that the first arriving HOM is LP02-like mode, while all other HOMs resemble LP11-like modes. It worth mentioning that the temporal enlargement of the FM peak on the spectrogram around 1064nm is caused by the presence of the pump peak at that wavelength and can lead to an additional temporal overlap between modes on the C^2 trace, affecting the ranges of the SM regime. A noteworthy advance of the flexible C^2 method, to the best of our knowledge, it is the only one technique that can spectrally resolve all three regimes of operation of the rod fibers.

7. Conclusion

We have demonstrated an unique versatility of the setup for the flexible cross-correlated imaging in the time domain. Its ultimate tunability in wavelength and bandwidth opens up new possibilities for advanced modal characterization giving new insights and benefits in the development of advanced fibers/waveguides. Being exceptionally adjustable the system allows to tune an input spectral shape and bandwidth and to scan along a wide range of wavelengths and being able to obtain a full overview of the modal behavior not only for a common fiber, but also for the fibers of specific design as it was shown on example of the DMF rod fiber.

An influence of the spectral shape and bandwidth on the appearance of the C^2 imaging trace was investigated by analyzing the modal content of SMF28. We noticed, that for wavelengths shorter than 900nm, the input spectrum of 8 merged beams is smoother than for longer wavelengths, especially approaching a wavelength of 1064nm, where the pump peaks causes the main disturbance. However, it was still possible to resolve the modal content of SMF28. It is noted that the reference fiber at wavelengths shorter than 920±30nm also support HOMs, but any influence from them on the results of the measurements was not noticed. Modes of SMF28 at the wavelength of 870nm close to the turn around point were detected and reconstructed by proposed in the paper an alternative method for the modal reconstruction with ability to extract an intensity and a phase distribution of the modes from a single interferogram. In the concept, the measurement can be provided even on a broader range of wavelengths, the only limitation is the operational range of wavelength for the setup components. To demonstrate an exceptional flexibility of the optimized setup for C^2 imaging we evaluated the modal content of the DMF rod fiber along a wavelength range from 1050nm to 1090nm and detected 3 regimes of the rod fiber operation. Investigation of the modal content below the SM regime with detailed modal reconstruction is presented.

Funding

Innovation Fund Denmark (Innovationsfonden) (0603-00514B).

Acknowledgment

The authors would like to thank Mette M. Jørgensen for her help with the simulations of the rod fiber.